Harnessing Embedded Magnetic Fields for Angular Sensing With Nanodegree Accuracy

Shaohui Foong, *Member, IEEE*, Kok-Meng Lee, *Fellow, IEEE*, and Kun Bai, *Student Member, IEEE*

Abstract—A multisensor approach that capitalizes on the existing magnetic fields in permanent-magnet-based actuators to achieve unobtrusive high-accuracy position sensing is presented. As magnetic-field models are position dependent, their inverse problems are often highly nonlinear with nonunique solution. This paper illustrates the principle and motivation for a multisensor approach using the concepts of parametric spaces to take advantage of multiple independent sensor measurements to induce a unique field-position correspondence in multisource fields. A direct mapping approach using supervised back-propagation artificial neural networks is utilized to attain positional information from distributed field measurements. Using an experimental rotary setup containing 24 magnetic sources, the measurements obtained from a network of magnetic Hall-effect sensors are statistically characterized and used to investigate the factors affecting the accuracy of the sensing system. Of particular interest are the combined effects of the number and spatial configuration of the sensors. Two types of sensor arrangement are investigated: an in-phase configuration consisting of evenly spaced sensors and a staggered configuration where unevenly spaced sensors concurrently measure different points of a periodic field. Using a network of 24 single-axis Hall-effect sensors in staggered configuration, the system is capable of achieving nanodegree angular positional accuracy.

Index Terms—Artificial neural networks (ANNs), electromagnetic devices, magnetic sensors, signal mapping.

I. INTRODUCTION

MAGNETIC sensors are commonly utilized as media for actuation and sensors. Sensing systems that operate on this principle are able to function in harsh conditions as magnetic fields are invariant to temperature, pressure, radiation, and other environmental factors. Harnessing magnetic fields for orientation/position sensing are not new as evident by Raab's *et al.* [1] magnetic tracking system introduced three decades ago. As compared to its other noncontact counterparts (such as optical [2] and vision-based sensors [3]) for real-time closed loop control of multidegree-of-freedom (DOF) dexterous devices such as those described in [4]–[9], magnetic sensors do not require "a line of sight" and permit sensing across multiple nonferromagnetic mediums. Despite major advancement in

miniaturization and magnetic sensing technology where modern sensors possess small physical footprints and high sensitivity and bandwidth [10], [11], the use of magnetic sensors for real-time feedback control of actuators and devices is under exploited. The main obstacle preventing widespread adoption of such magnetic field-based noncontact sensors is the complexity involved and nonuniqueness encountered in determining the orientation/position of the permanent-magnet (PM) with field measurements from the sensors. Inspired by developments in sensor fusion and sensing networks, a nontraditional multisensing approach for PM-based actuators [4]–[9] and magnetic tracking applications [12]–[19] is pursued.

It is desired that this sensing system requires minimal additions or modifications to the actuator to provide feedback. This notion provides the impetus for the development of a multisensor system for electromagnetic devices that uses the existing assembly of high-coercive rare-earth PMs to concurrently provide both actuation and sensing feedback. In general, a field is a physical quantity associated with every point in space (or time). The notion of control-oriented distributed field sensing is twofold. The first is to capitalize on the incidence of existing fields in dynamic systems for efficient and unobtrusive position sensing. Given a set of instantaneous field measurements, the second is to provide positional estimates accurately and swiftly (low computational lag) as feedback for closed-loop control.

The main difficulties in cultivating position-field correspondence are the complexities of analytical field models and the absence of bijectivity (both injective and surjective or encompassing one-to-one and onto correspondence) between field measurements and position/orientation. Also known as the magnetic "inverse problem," contemporary literature has labeled this class of quandary being "highly nonlinear and without formulations to follow" [14], as well as "not solvable uniquely, even with complete knowledge of. . .magnetic field everywhere" [15]. In a nonbijective relationship, multiple positions/orientations share a common field measurement value. However, in a bijective relationship each field measurement is associated with only one position or orientation. It is clear that without bijection, associating an arbitrary field measurement with a unique position is difficult.

Another critical issue is the manner and speed of extracting position/orientation from field measurements to satisfy the stringent requirements of feedback control. While theoretical field models for the prediction of fields in space are available, they are often highly complex and not in a tractable form for direct inverse computation operations, requiring inefficient nonlinear optimization methods [16]–[18]. Moreover, model predictions and actual field measurements can differ and these

discrepancies can significantly hamper the consequential sensing accuracy. However, even if these models are highly accurate and computation speed is not an issue, the symmetry inherent in all fields impedes bijectivity between measurements and position [19]. This concern is exacerbated in systems with multiple field sources.

The remainder of this paper offers the following.
1) We discuss the principle of a field-based sensing system that harnesses the attached magnetic field of a body undergoing nonrelativistic motion for noncontact position sensing with multiple sensors.
2) To address practical issues encountered in implementing a field-based sensing system, we present a model-independent approach that capitalizes on concurrent and independent field measurements to create a bijective relationship between measurement and position parametric spaces. A direct mapping approach of using artificial neural networks (ANNs) is employed to swiftly and accurately relate measurements to position.
3) A single-DOF rotary setup containing 24 magnetic sources and sensors is presented as an experimental platform to investigate and highlight the factors such as mapping model, order and domain, number of sensors, and spatial configuration of a network that affect the accuracy of the system. Two spatial configurations are examined: an in-phase and staggered arrangement where sensors measure the same and different points of a periodic field, respectively. In staggered sensor configuration, the system was able to attain nanodegree angular positional accuracy.

II. SENSING MODELS USING EMBEDDED MAGNETIC FIELDS

Apart from the physics governing the behavior of a field in motion, developing a sensing system to track a moving body with an attached field requires the following considerations.
1) A heuristic method to classify the field in parametric spaces where bijective (one-to-one and onto) relationship between the measured magnetic field and the position/orientation holds.
2) A scheme to precisely associate the measured field with the position and/or orientation coordinates without time-consuming computation.
3) Dealing with multisource fields and practical implementation issues such as natural variation among field sources.

The aforementioned considerations are best illustrated with an example shown in Fig. 1(a), where a physical body containing magnetic sources in a system is described by the xyz coordinate frame (origin $\mathbf{O}$). Using the Euler notation, the orientation of the moving xyz frame is described by a sequence of body-fixed rotations about x-, y-, and finally z-axes by the corresponding angles of α, β, and γ, respectively. For the magnetic field in a source-free and current-free space $\mathbf{\Omega}$ satisfies Maxwell's equations, the propagation of the moving magnetic field can be described by the homogeneous vector wave equation [20]:

$$\nabla^2 \mathbf{B} - \frac{1}{c_o^2}\frac{\partial^2 \mathbf{B}}{\partial t^2} = 0 \text{ where } c_o = 1/\sqrt{\mu_o \varepsilon_o}. \quad (1)$$
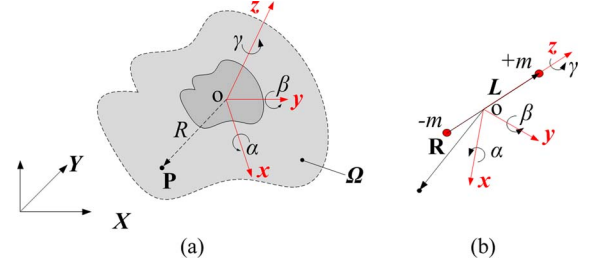

Fig. 1. Describing a moving body with the attached field. (a) Source-free and current-free space. (b) Single dipole model.

In (1), $\mathbf{B}$ is the magnetic flux density and c_o represents the speed of magnetic wave propagation (or light) in free space. Taking into account the observation distance R, the measured $\mathbf{B}$ at a stationary point $\mathbf{P}$ in $\mathbf{\Omega}$ can be expressed [21] as

$$\mathbf{B_P}(t) = \lim_{R/c_o \to 0}\left[\mathbf{B_P}(t - R/c_o) + \frac{R}{c_o}\frac{\partial \mathbf{B_P}(t - R/c_o)}{\partial t}\right]. \quad (2)$$

The first term in (2) follows directly from the propagation delay, and the second component accounts for the delayed change in field due to spatial rotation. Equation (2) implies that for most electromechanical systems considered here (where $\mathbf{P}$ is close to the radiating body), the time scale R/c_o is in the order of nanoseconds validating the quasi-static assumption; in other words, the magnetic field in $\mathbf{\Omega}$ is invariant to time and only dependent on the spatial angles (α, β, γ):

$$\mathbf{B_P} = \mathbf{B}(R, \alpha, \beta, \gamma). \quad (3)$$

This property permits the direct correspondence between magnetic field measurements and position/orientation for dynamic systems undergoing nonrelativistic motion.

Consider the moving body containing a single PM modeled as a single dipole [20] (with field strength m and source-sink separation L) fixed onto the z-axis and centered about $\mathbf{O}$ as shown in Fig. 1(b). By the principle of superposition, the measured $\mathbf{B_P}$ (or flux density) at point $\mathbf{P}$ with respect to the fixed xyz frame is given by (4) in nondimensional form

$$\frac{\mathbf{B_p}}{m\mu_o/(4\pi L^2)} = \tilde{\mathbf{B}}_\mathbf{p} = \frac{\rho\vec{\mathbf{R}} - \vec{\mathbf{L}}/2}{|\rho\vec{\mathbf{R}} - \vec{\mathbf{L}}/2|^3} - \frac{\rho\vec{\mathbf{R}} + \vec{\mathbf{L}}/2}{|\rho\vec{\mathbf{R}} + \vec{\mathbf{L}}/2|^3}. \quad (4)$$

In (4), $\vec{\mathbf{R}}$ is the unit vector relating the directionality of $\mathbf{P}$ with respect to $\mathbf{O}$, $\vec{\mathbf{L}}$ is the unit vector relating the inclination of the dipoles in space, and $\rho = R/L$ is the aspect ratio of the measurement at $\mathbf{P}$. As the dipoles are placed on the z-axis, $\mathbf{B_p}$ is only sensitive to α, β and independent of γ.

A. Forward and Inverse Parametric Space

The dimensionless measured $\tilde{\mathbf{B}}_\mathbf{p}$ in (4), which is a function of the direction $\vec{\mathbf{R}}$ and the rotation angles (α, β), can be presented using three distinct plots in the forward parametric space Σ (set of all unique orientation), where measured data are expressed in terms of the positional coordinates (α, β). As a visual representation, Fig. 2(a) simulates measured $\tilde{\mathbf{B}}_\mathbf{p}$ for $\vec{\mathbf{R}} = \begin{bmatrix} 1 & 0 & 0 \end{bmatrix}^\mathrm{T}$
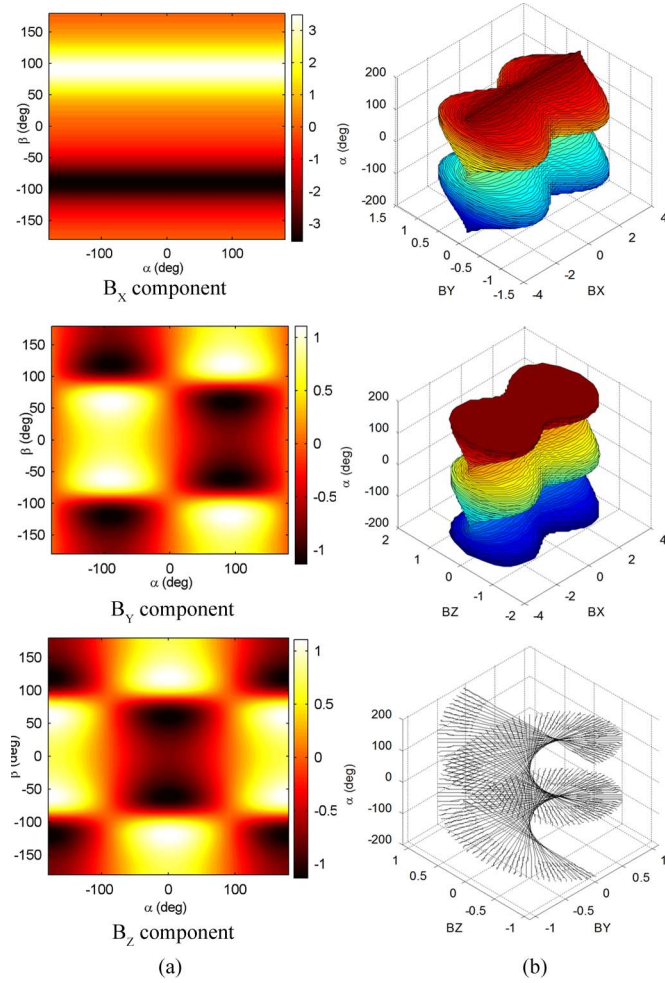
This article has been accepted for inclusion in a future issue of this journal. Content is final as presented, with the exception of pagination.

FOONG *et al.*: HARNESSING EMBEDDED MAGNETIC FIELDS FOR ANGULAR SENSING WITH NANODEGREE ACCURACY   3

Fig. 2. Field measurements in parametric space. (a) Forward parametric model. (b) Inverse parametric model.

Fig. 3. Field classification in forward model parametric space.

the inverse parametric space Λ (set of all unique λ) for α corresponding to Fig. 2(a). Unlike the forward parametric space, the domain of the inverse parametric space is not well defined. As both spaces are equivalent, analysis of the forward parametric space is used to draw insights and conclusions in the inverse parametric space.

B. Bijective Inverse Model Relating λ and q

Mathematically, if the forward model f is bijective, the inverse model f^{-1} exists and is bijective as well. This property allows measurements to be mapped uniquely to position/orientation coordinates, which is the fundamental mechanics of a sensing system. Fig. 3 illustrates a visual approach to locate and determine bijective domains in the forward parametric space where by definition f will be bijective as well.

Through observation of the field distribution in the forward parametric space Σ and noting well-defined segmentation, the forward parametric space in Fig. 2(a) can be segregated in 4×4 grid with 16 *equal* sectors as shown in Fig. 3. In Fig. 3, each sector is referenced by the signs of the three **B** components in $\lambda = [B_{PX}\ B_{PY}\ B_{PZ}]^T$. To facilitate identification, each sector is referenced using the column and row index. As there are three sensing axes at **P**, only up to 2^3 sectors can be uniquely described. Hence, the entire parametric space is not *bijective* (encompassing one-to-one and onto correspondence); f^{-1} does not exist for the entire space. For example, the field maps for all three axes in sectors (1, 1) and (2, 3) are identical; it is not possible to uniquely distinguish between the two sectors. As will be explained in the next paragraph, this shortcoming limits the working range of a single three-axis sensing system.

However, subsets of the entire parametric space are bijective and determining such spaces is achieved directly from the classified space in Fig. 3. Using all three sensing axes, one possible bijective subdomain is defined by $\alpha \in (-\pi, \pi)$ and $\beta \in (-\pi/2, \pi/2)$ where all eight sectors are uniquely referenced by the sign of λ. With two sensing axes, only up to 2^2 sectors can be uniquely described. One possible subdomain (bijective to B_X and B_Y) is $\alpha \in (-\pi/2, \pi/2)$ and $\beta \in (-\pi/2, \pi/2)$.

using (4), where points with positive $\tilde{\mathbf{B}}_{\mathbf{p}}$ are shaded lightly and vice versa.

In Fig. 2(a), the axes of this Cartesian parametric space are the individual components of the position/orientation vector $\mathbf{q} = [\alpha,\ \beta]^T$ and the value at each point in space is a singular component of the field measurement vector $\lambda = [B_{PX}\ B_{PY}\ B_{PZ}]^T$. This parametric space Σ is a basis of the *forward* model that characterizes the field with respect to the individual components of $\mathbf{q}$. As other field models exist (such as the distributed multipole (DMP) model [22], [23]) and to account for multisource fields, without loss of generality, a forward model can be denoted by the function f, and it can be mathematically presented as

$$f : \mathbf{q} \in \Re^2 \rightarrow \lambda \in \Re^3. \tag{5}$$

Field-based position/orientation sensors require an *inverse* model that solves for the position/orientation of the moving coordinate frame from measured $\mathbf{B}_{\mathbf{p}}$. Essentially, the inverse expression of (5), f^{-1}, is necessary and sufficient for field-based sensing. Even with a single dipole model, extracting an analytical expression for $\mathbf{B}_{\mathbf{p}}^{-1}$ is difficult due to the highly coupled nature and high degree of nonlinearity in (4). Fig. 2(b) plots
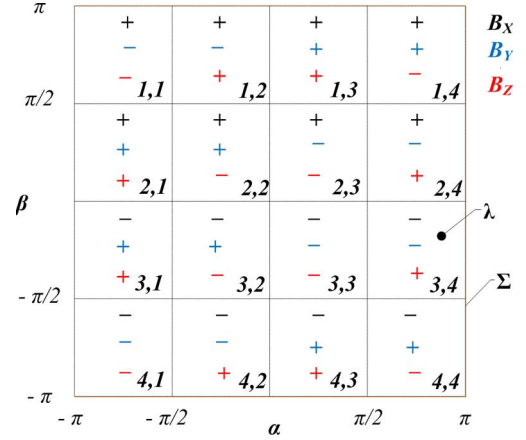
In summary, bijection depends on both the function f and the domain space of Σ. In addition, this segregation, due to the orthogonality and independence of field measurements, is not limited to a single sensing location but extendable to multiple sensing axes of other sensors as well.

C. Mapping in Inverse Parametric Spaces

While parametric space analysis guarantees a unique correspondence between field measurements and orientation/position, a method of computing $\mathbf{q}$ from λ is required. As inverse computation of orientation from field measurements using analytical models (solving for f^{-1}) is not tractable, computationally intensive and unsuitable for real-time feedback, a function-fitting approach is adopted. With this mapping approach, the desired inverse model relationship f^{-1} is approximated by a fitted analytical artificial function. Lookup tables (LUT) and conventional least squares (LS) using basis functions of polynomials and sinusodials are commonly used methods in creating such mappings but ANN mapping is preferred as the latter are more adaptable and scalable when managing multiple inputs and outputs.

Paired with supervised learning, back-propagation ANNs are used to fit a desired set of inputs to a corresponding set of outputs by iteratively adjusting the weighting coefficients in the network. A commonly used cost function is the root mean-squared error (RMSE) that tries to minimize the square root of the average squared error between the network's outputs and the desired target values over all data pairs. The order of the network is easily controlled by the number of hidden layers g and number of hidden nodes h within each layer.

In order to map field measurements λ to the angular positions of $\mathbf{q}$ in the 2-DOF case, the selected bijective domain of the forward parametric space is discretized into an $N_1 \times N_2$ spatial grid, resulting to total of $N_1 N_2$ ANN training-target sets. For field mapping using the ANN, 80% of the sets will be used for training, 15% for validation, and 5% for testing. For this application, the inputs of the neural network (g hidden layers and h hidden nodes per hidden layer) are field measurements by all sensors and the outputs are the target position. This can be mathematically represented as

$$\hat{\mathbf{q}}_v = \mathbf{NN}_{g,h}\left(\lambda(v)\right) \tag{6}$$

where v is an integer representing the training set index ($1 \leq v \leq N_1 N_2$), and $\hat{\mathbf{q}}_v$ is the angular estimates of the neural network. The RMSE is used to evaluate the performance of a neural network and is expressed as

$$\text{RMSE} = \sqrt{\frac{1}{N_1 N_2} \sum_{v=1}^{N_1 N_2} [(\alpha_v - \hat{\alpha}_v)^2 + (\beta_v - \hat{\beta}_v)^2]}. \tag{7}$$

Clearly, the resolution of this map, choice and number of ANN inputs, and order of ANN have a direct impact on the overall mapping accuracy.

D. Periodic Fields in a Multisource System

Few physical systems contain isolated single magnetic sources and multi-DOF electromagnetic actuators [4]–[9] feature an assembly of multiple PMs in a concentric pattern about the z-axis (or axial) on the moving body. The spinning motion or change in γ can be detected by sensors in Ω. However, an undesirable effect of such multi-PM configurations is the presence of multiple magnetic sources that introduces periodic nature of the resultant field along the γ spin axis. For a symmetric multi-source system producing a periodic field (with spatial period Φ) about the z-axis of the system, the forward parametric space can be discretized into equal indistinguishable segments. Hence, instead of mapping the entire space, only characterization of the segment space is required.

In practical applications, inevitable field disparities exist between segments in homogenous PM assemblies due to source strength variation and other physical imperfections. A direct method to compensate for these effects is to implement affine transformation (AT) on field measurements of all segments with respect to a chosen "reference" segment. For single-axis sensors, the AT consists of scaling and translation factors. These factors will be chosen through optimization such that the field measurements in transformed segments will resemble the reference segments in the LS sense.

The segment AT of the n_{th} segment of the sth sensor can be expressed by

$$\widehat{\mathbf{B}}_{(n,s)} = \mathbf{a}_{n,s}\mathbf{B}_{(n,s)} + \mathbf{b}_{n,s} \tag{8}$$

where $\mathbf{a}_{n,s}$ and $\mathbf{b}_{n,s}$ are the linear transformation and translational factors of the AT for the n_{th} segment of the s_{th} sensor. These factors are optimally chosen such that the following error function is minimized:

$$\|\widehat{\mathbf{B}}_{(n,s)} - \bar{\mathbf{B}}_{(r,s)}\|_2^2 \tag{9}$$

where $\bar{\mathbf{B}}_{r,s}$ is the LS- or ANN-fitted model of the r_{th} segment of the s_{th} sensor.

III. Practical Issues, Results, and Discussion

Physical fields exhibit symmetry and in systems with multiple field sources, field periodicity occurs. In practice, perfect symmetry and periodicity do not materialize due to physical imperfections originating from sources and sensors. This sensing method introduced here takes advantages of the experimental statistical field variations in both sources (PMs) and sensors to uniquely determine position from distributed field measurements. As a basis for comparison, field-based sensing utilizing simulated magnetic field measurements from analytical field models is presented as well. This novel concept is best illustrated experimentally using a single-DOF rotational system. The setup demonstrates the principle of the design and identifies factors that significantly influence mapping accuracy between field measurements and position.

Fig. 4 illustrates the multisource-multisensor (MSMS) system in Fig. 5 for investigating the effects of redundant sensors, AT, and the following design factors on the measuring accuracy of its spin motion about the Z-axis; variations in sources
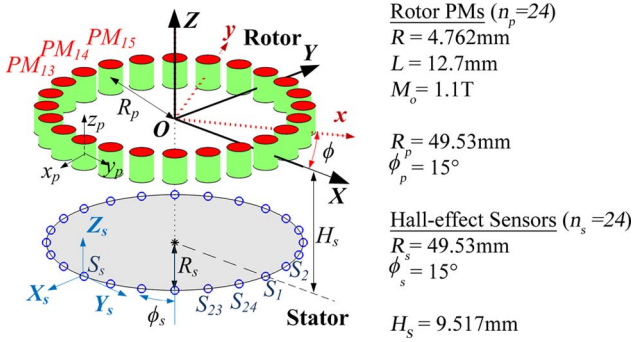
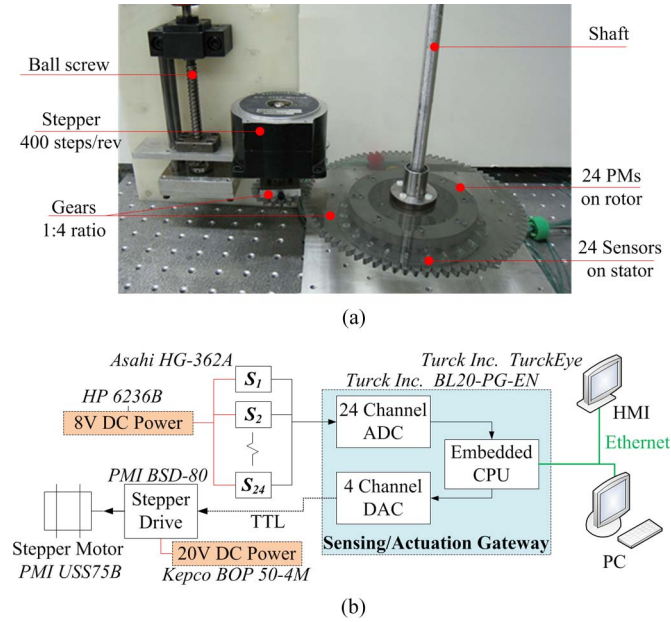Fig. 4. Rotating multi-PM assembly and stationary sensor placements.

Fig. 5. Experimental setup. (a) Overview. (b) Electrical and communication schematics.

and sensors, mapping methods and algorithms (type and order) for determining the local and global field-position, and sensor configurations.

In Fig. 4, n_p (axially magnetized, cylindrical) PMs are evenly spaced (with angular spacing ϕ_p) in a circular fashion (of radius R_R) on a circular plate rotor; and n_s single-axis sensors (denoted as S_s in Fig. 4) are rigidly placed (with angular spacing ϕ_s) on a circular path (of radius R_s) below the plate rotor for measuring the z-component of the magnetic field. The PMs (with their magnetization vectors parallel to the $-Z$ axis) are numerically indexed in a counterclockwise manner such that the x- and y-axes of the rotor-fixed coordinate frame pass through the midpoints between PM_1 and PM_{24} and between PM_{18} and PM_{19}, respectively. As a result, the spatial periodicity Φ of this 24-PM assembly is 15°. Similarly, the sensors are numerically indexed but defined such that the X- and Y-axes of the stator-fixed reference frame pass through S_1 and S_7, respectively.

A. Magnetic Field Data Collection of the MSMS System

The data collection system is shown in Fig. 5(b), where the analog voltages of the field measurements acquired by the Hall-effect sensors are digitized by 24 independent 16-bit Delta Sigma analog-to-digital converters (ADCs), and communicated to a human machine interface (HMI) and a PC over Ethernet connection to provide instantaneous display and data logging capabilities. To automate the data collection process, a stepper/gear motion system with an effective resolution of 1600 steps/rev (or 0.225° per step) was designed as shown in Fig. 5(a), where the ball screw provides accurate adjustment of the separation H_s between the rotor PMs and sensors. With a sensing/actuation gateway containing a 32-bit RISC and 100BASE-TX Ethernet connectivity attached to the digital-to-analog converter (DAC) banks and a custom C program running on the PC, measurements were automatically collected by the 24 sensors as the stepper motor increments.

Fig. 6(a) shows a typical set of measurements taken by S_1 as the 24-PM assembly rotates one revolution, which represents the forward parametric space of the single-sensor system. To facilitate the discussion, the data measured by S_1 are plotted against the DMP model [22], [23] based on manufacturer's specified magnetization M_o in Fig. 6(a), where the cylindrical PM is mathematically modeled by seven dipoles (or a pair of source and sink separated by a distance l) with strength m_i ($i = 0, 1, \ldots, 6$) in parallel to its magnetization vector. The magnetic flux density $\mathbf{B_p}$ at the measured point $\mathbf{p}$ due to a single PM can then be simulated using the DMP model

$$\mathbf{B_p} = \frac{-\mu_o}{4\pi} \sum_{i=0}^{6} \left[m_i \left(\frac{\mathbf{p} - \mathbf{P}_{i+}}{|\mathbf{p} - \mathbf{P}_{i+}|^3} - \frac{\mathbf{p} - \mathbf{P}_{i-}}{|\mathbf{p} - \mathbf{P}_{i-}|^3} \right) \right] \quad (10)$$

where $\mathbf{P}_{i+}$ and $\mathbf{P}_{i-}$ are the position coordinates of the source and sink of the ith dipole; and μ_o is the permeability of free space. For the PMs in Fig. 5, $l = 9.102$ mm; $m_0 = -1.340 \times 10^{-6}$ A/m (center of cylinder); $m_1 = m_2 = \cdots = m_6 = 2.03 \times 10^{-5}$ A/m (distributed evenly on a circular path with a radius of $a = 2.4$ mm about m_0).

Several observations can be made as follows.

1) As compared in Fig. 6(a), the measured data closely agree in-phase with the DMP model suggesting that individually the PMs are uniformly magnetized axially. This implies that the 24-PM assembly with a spatial periodicity of 15° can be divided into 24 segments.

2) Variations in the sinusoidal magnitudes, particularly at the troughs where the sensors are closest to each PM, reveals the 24 (supposedly identically graded) PMs do not have a uniform M_o. Fig. 6(b) provides a statistical visualization of the effect of M_o variations on the measured fields in each segment; on each box, the central mark is the median; the bottom and top edges of the box are the 25th and 75th percentiles, respectively; and the whiskers extend to the most extreme data points.

3) With 24 sensors, a similar boxplot can be constructed for visualizing the effect of sensor variations on the measured field across all 24 segments (or PMs). As shown in
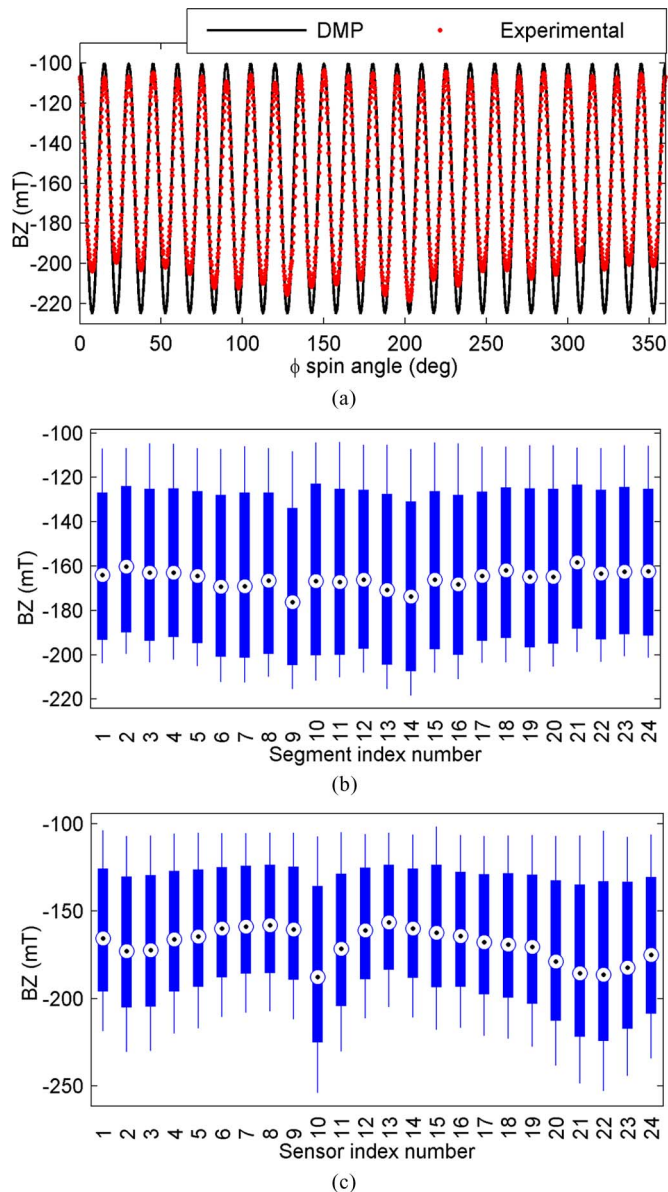
This article has been accepted for inclusion in a future issue of this journal. Content is final as presented, with the exception of pagination.

6

IEEE/ASME TRANSACTIONS ON MECHATRONICS

Fig. 6. Field measurements by sensors. (a) Measured and modeled field by S_1. (b) Measured field variation across segments by S_1. (c) Measured field variation across all 24 sensors.

Polynomial with k^{th} order (Single sensor, S_1)					
Order (k)	Cubic	4th	5th	6th	7th
RMSE (deg)	0.1453	0.1443	0.1061	0.1050	0.0897
ANN with single hidden layer of h nodes (Single sensor, S_1)					
Nodes (h)	3	4	5	6	7
RMSE (deg)	0.0887	0.0832	0.0827	0.0810	0.0797
ANN with single hidden layer with h=2 nodes (Multi sensors)					
# of S_i	1	2	4	8	16	24
S_i	S_1	S_1, S_2	$S_1, ..., S_4$	$S_1, ..., S_8$	$S_1, ..., S_{16}$	$S_1, ..., S_{24}$
RMSE	0.1299	0.1149	0.0992	0.0679	0.0620	0.0295

map can be constructed using a polynomial model or an ANN as illustrated in Table I. However, the latter is better suited for a multi-DOF and/or multi-input system as it can concurrently map all sensors in the reference segment to a specific orientation—an advantage not effortlessly realizable with a polynomial model. Table I illustrates the effects of two fitting methods for constructing the position-field mapping in Segment 1 ($0 \leq \phi \leq 15°$).

1) A polynomial of k order (single sensor S_1 only).
2) An ANN with a single hidden layer of h nodes.
    a) Single sensor S_1.
    b) Multiple sensors (equal spacing of 15°).

As a basis for comparison, the numbers of k order and h nodes range from 3 to 7 with measured data from sensor S_1. Unlike a polynomial fit, the ANN is a single-output (ϕ angle) but multi-input (one for each sensor) utilizing information from multiple segments to the reference. In the following, only ANN is considered. In addition, the findings in Table I show that the inclusion of more sensors for field-position mapping results in lower RMSE. For the same number of hidden nodes, the ANN with 24 sensor measurements demonstrates a lowest RMSE of 0.0295° or about an order-of-magnitude better than that with only sensor S_1.

The aforementioned ANN mapping can be used to derive the field-position correspondence for a "reference" segment (that has the segment's median closest to the aggregate median). Along with the statistical boxplot in Fig. 6(b), the reference map provides a basis to determine the field-position correspondence for the global domain ($0 \leq \phi \leq 360°$) taking into account the nonuniformity in the sources and sensors. In this approach, the AT is utilized to statistically "standardize" all segments with respect to this reference for use on other transformed segments. An incremental indexer or absolute classifier is needed to keep track of the current segment location.

For the data in Fig. 6, Segment 1 (median of -164.92 mT) was chosen as the reference segment. The estimation errors $|\hat{\phi} - \phi|$ resulting from using the reference map (created using S_1) on other segments with AT are plotted in Fig. 7, and are categorized in Table II with respect to their segment origin and the RMSE of the estimation error computed and aggregated for a more in-depth understanding. To help visualize the effect of source variations, the breakdown of the RMSE in each segment for sector mappings is compared against two other approaches in Table II: 1) without AT; all segments/PMs assumed identical. 2) Each segment is individually mapped using dedicated ANNs and measurements from all 24 sensors.

The following insights can be gained from the findings.

Fig. 6(c), each of the 24 identically graded sensors has different characteristics.

4) As observed in Fig. 6(a), the association between field measurement and position for a single-sensor measurement is *bijective* only within half a segment. Indiscriminate mapping of the entire 360° rotation due to lack of bijection will cause erroneous results [24]. To address this issue, a combination of reducing the mapping domain and utilization of additional sensors is investigated.

B. Effect of Mapping Methods on RMSE Within a Segment

To determine the correspondence between the measured field and the angular position for a limited motion range presented by one segment, an LS fit model of the field is sought to minimize the effects of measurement noise. For a single-DOF case, this

This article has been accepted for inclusion in a future issue of this journal. Content is final as presented, with the exception of pagination.

FOONG *et al.*: HARNESSING EMBEDDED MAGNETIC FIELDS FOR ANGULAR SENSING WITH NANODEGREE ACCURACY 7
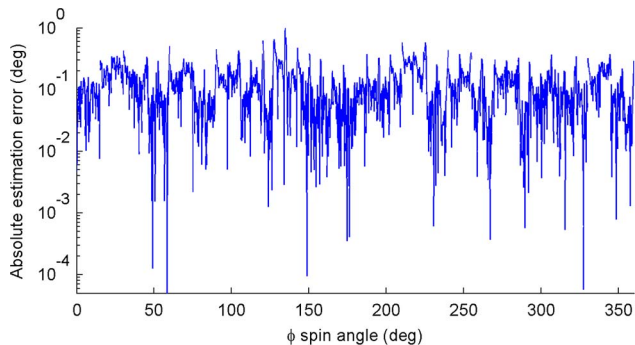
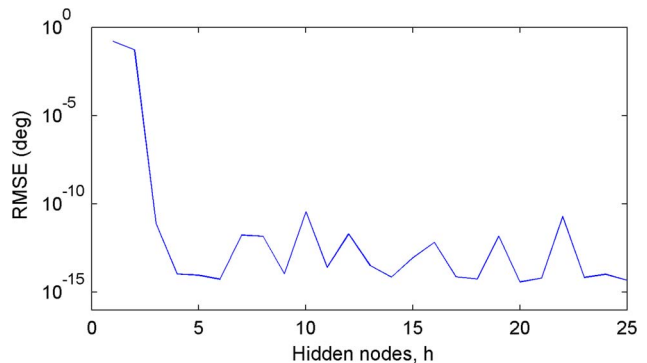Fig. 7.   Estimation error (AT with Segment 1 as a reference).

Fig. 8.   Effect of hidden nodes (single hidden layer, $g = 1$).

TABLE II
EFFECT OF MAPPING MODELS ON RMSE ($h = 3$)

Segment	Root Mean Squared Error (deg)		
	ANN (only S_1)		ANN ($S_1,...,S_{24}$)
	No AT	With AT	
1 (Ref)	0.0887		9.15×10^{-10}
2	0.4455	0.2153	6.95×10^{-12}
3	0.2024	0.1741	1.72×10^{-10}
4	0.2367	0.1143	6.76×10^{-11}
5	0.2564	0.1785	1.16×10^{-10}
6	3.2981	0.3019	5.57×10^{-13}
7	3.2997	0.1822	1.39×10^{-11}
8	1.7985	0.1122	1.59×10^{-10}
9	8.6133	0.3410	5.43×10^{-12}
10	2.7710	0.1777	2.26×10^{-13}
11	1.9712	0.0816	4.34×10^{-10}
12	0.9831	0.0876	2.81×10^{-13}
13	8.7933	0.1141	4.88×10^{-13}
14	20.4310	0.1241	5.42×10^{-10}
15	0.9977	0.2794	8.42×10^{-12}
16	2.2434	0.1350	6.38×10^{-13}
17	0.1534	0.1472	6.52×10^{-9}
18	0.1025	0.0733	2.87×10^{-11}
19	0.7504	0.1553	5.47×10^{-10}
20	0.2794	0.0674	2.36×10^{-10}
21	0.4154	0.1104	1.41×10^{-12}
22	0.1068	0.0954	3.25×10^{-10}
23	0.3727	0.1793	1.71×10^{-10}
24	0.2405	0.0840	9.58×10^{-11}
Max	20.4310	0.3410	6.52×10^{-9}
Min	0.0887	0.0674	2.26×10^{-13}
Mean	2.4522	0.1422	4.31×10^{-10}
SD	4.5186	0.0666	1.317×10^{-9}

1) This approach significantly simplifies the mapping process (requiring fewer hidden nodes) since the segment domain required for characterization is a fraction of the global domain. As shown in Fig. 8, the ANN mapping using all 24 sensors requires a single hidden layer with 3 nodes to reach an RSME of less than 10 nanodegrees. For the system considered here, each segment represents slightly less than 5% of the total global map.

2) For the case of a single sensor, AT has a significant impact on the overall RMSE, lowering each segment's RMSE and reducing the entire RMSE by at least an order of magnitude. Without AT, the substantial field variation in Segment 14 instigated an RMSE of more than $20°$. However, with AT, the maximum RMSE has been radically reduced to $0.341°$. The average RMSE for the global domain without AT is $2.4522°$ but it is reduced to $0.1422°$ with AT.

3) Unlike the approach using a reference segment mapping with AT, the use of 24 dedicated ANNs with 24 sensors has the capability to achieve nanodegree accuracy. While the approach demands more memory space for all the networks, the fact that each ANN requires only a few hidden nodes represents a significant advantage.

C. Effect of a Sensor Phase on Global Field-Position Correspondence

Fig. 9(a) illustrates two different configurations of sensor placement for a system with n_p evenly spaced PMs with measured data given in Fig. 9(b) and (c) where $n_s = n_p = n = 24$. The rationales behind the design are as follows.

1) *In-phase*: The PMs and sensors have the same angular spacing of $360°/n_p$. For the sinusoidal field (with periodicity of $\Delta = 360°/n_p$), all the n_s sensors measure the field at the same relative spin angle within its segment as shown in Fig. 9(b), where each of the 24 curves represents the data measured by a specific sensor. If all the sources and sensors are truly identical, all the data would collapse into a single sinusoidal curve.

2) *Staggered*: For n_p evenly spaced PMs, the n_s sensors are placed such that together they form a complete sinusoidal field. For $n_p = n_s = n = 24$, the spacing between two adjacent sensors is $15°$ as illustrated in Fig. 9(a). Unlike the in-phase placement where the measured data characterize the sensor variations at a specified spin angle, the 24 data of the staggered placement (when measured at a specified spin-angle) offer a spatial snapshot of the sinusoidal field as shown in Fig. 9(c). The advantage of this configuration is that even if all the sources and sensors are identical, they will not collapse into a single curve but a series of shifted periodic curves.
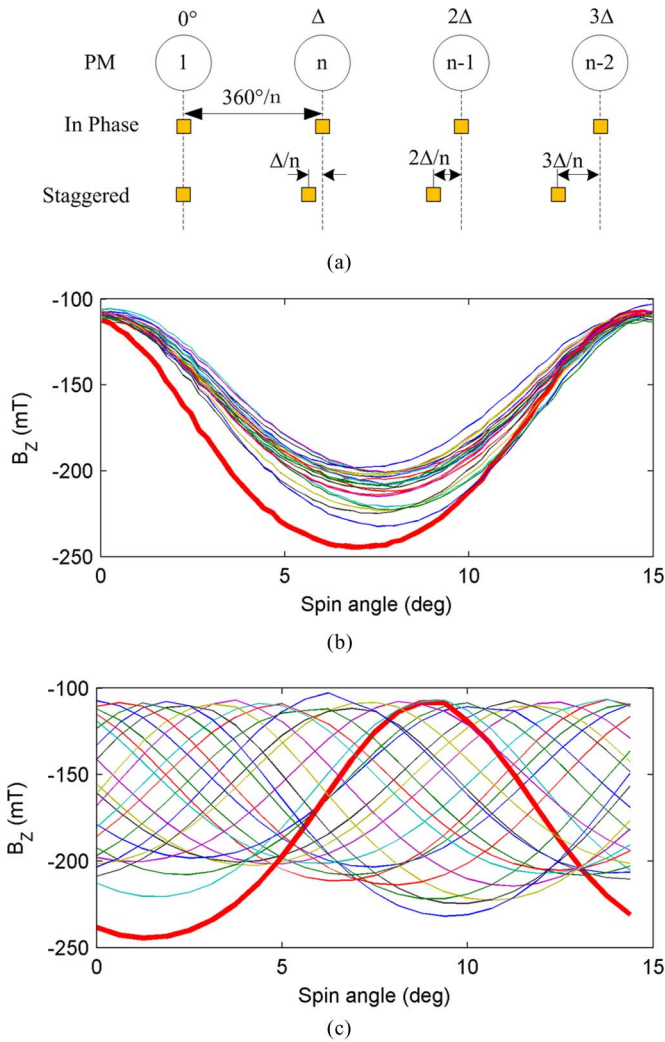
This article has been accepted for inclusion in a future issue of this journal. Content is final as presented, with the exception of pagination.

8   IEEE/ASME TRANSACTIONS ON MECHATRONICS

(a)

(b)

(c)

Fig. 9. Two types of sensor placement ($n_p = n_s = n = 24$, $\Delta = 15°$): in-phase and staggered configurations. (a) In phase and staggered configuration. (b) Field measurements by in phase configuration. (c) Field measurements by staggered configuration.

(a)

(b)

(c)

(d)

Fig. 10. Factors affecting mapping accuracy. (a) Segment, in-phase. (b) segment, staggered. (c) Global, in phase. (d) Global, staggered.

(a)

(b)

Fig. 11. Spatial distribution of mapping errors. (a) 15° segment map. (b) 360° global map.

The effects of sensor configurations on the accuracy of the two different mappings are presented in Figs. 10(a)–(d) and 11, which graph the RMSE against the number of hidden nodes, h, used in the single-layer ANN mapping, and the absolute mapping errors against spin angles, respectively. The results comparing the in-phase and staggered configurations are organized as follows.

1) Effect of number of sensors and hidden nodes on RMSE:
   a) 15° segment map; Fig. 10(a) and (b);
   b) 360° global map; Fig. 10(c) and (d).
2) Absolute mapping error ($n_s = 16, 24$):
   a) 15° segment map; Fig. 11(a);
   b) 360° global map; Fig. 11(b).

In Fig. 11, solid lines and dashed lines denote 24 and 16 sensors, respectively.

Significant findings are summarized from these results.

1) As the 15° segment map is significantly smaller than the global map, fewer sensors and hidden nodes are required to achieve the accuracy of 100 microdegrees for
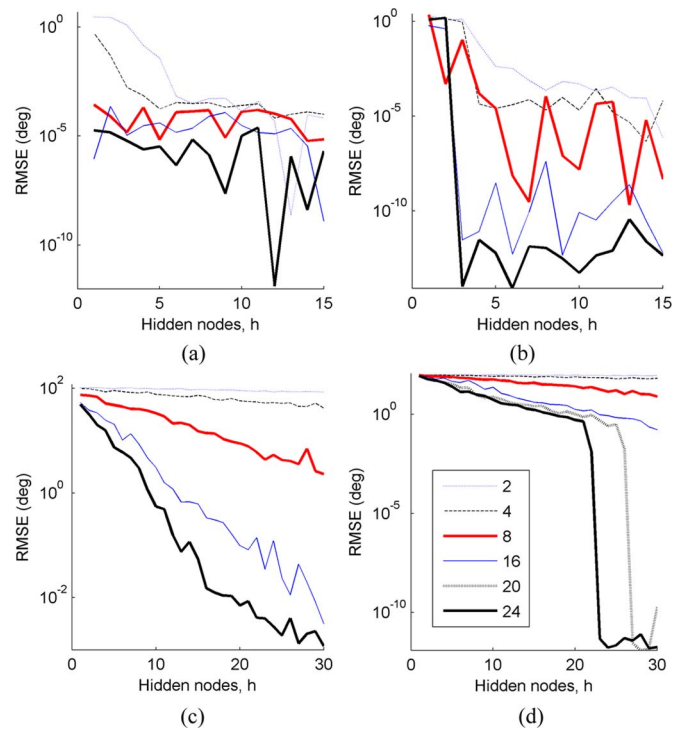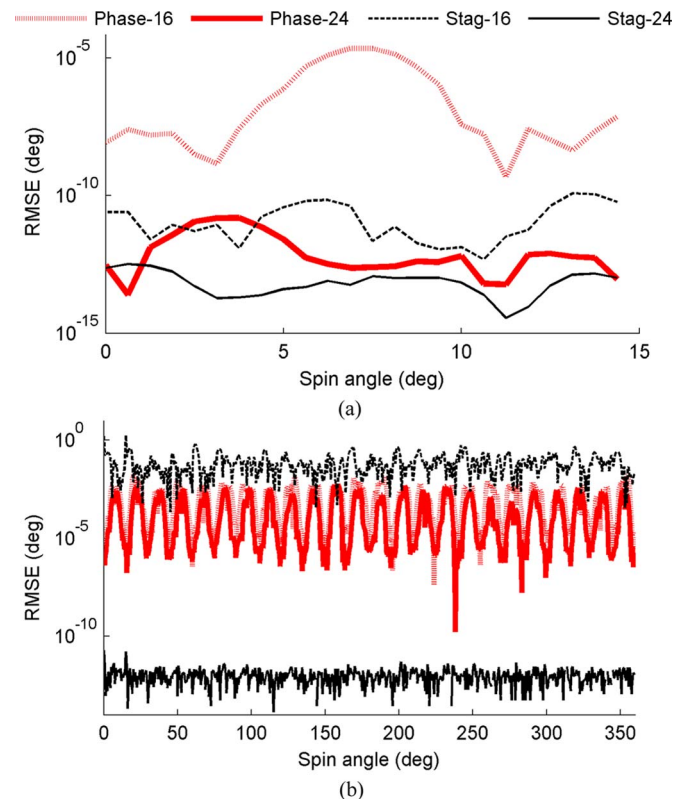
This article has been accepted for inclusion in a future issue of this journal. Content is final as presented, with the exception of pagination.

FOONG *et al.*: HARNESSING EMBEDDED MAGNETIC FIELDS FOR ANGULAR SENSING WITH NANODEGREE ACCURACY

9

both in-phase and staggered designs. However, unlike in-phase design where little or no improvements were found by increasing the number of in-phase sensors, the RMSE decreases drastically as the number of staggered sensors increases suggesting that the staggered placement provides a more effective means to characterize the nonlinear mapping between measured field and angular position.

2) In the case of global map, the in-phase sensor system using four or fewer sensors results in RMSE of almost $100°$, and increasing h has minimal impact. This occurs in the staggered sensor systems as well.

3) Although the effect of h becomes more pronounced when more than 16 in-phase sensors are used, the reduction in RMSE is limited to about $0.01°$. On the other hand, the RMSE rapidly reduces to less than 0.1 nanodegree once the combination of staggered sensors and hidden nodes exceeds a certain threshold. This phenomenon of a rapid reduction in RMSE is not observed in the in-phase case where all its data would collapse into a single sinusoidal curve if all the n_s sensors are truly identical.

4) Across both domains as shown in Fig. 11(a) and (b), increasing the number of sensors and favoring the staggered configuration results in lower absolute errors. For the same number of sensors, the absolute errors for the staggered case is lower than the corresponding in-phase case. This is especially apparent in the global domain when using 24 sensors where the improvement of using the staggered configuration is more than six orders smaller than that of the in-phase configuration.

These observations suggest that if the ANN (with 16 or more staggered sensors) has enough inputs, and is of sufficient order, it is able to characterize the mapping almost exactly.

IV. CONCLUSION

Employing pre-existing embedded fields for sensing has numerous advantages and a method to use distributed field measurements for high accuracy orientation sensing has been presented. This methodology addresses the difficulties encountered in magnetic inverse problems of high nonlinearity and nonuniqueness through analysis and characterization of the forward parametric space. In addition, this approach is model independent and uses a computationally swift function-fitting approach (ANNs) to directly map measurements to orientation of the system. The factors that affect the overall accuracy of the sensing system were investigated using an MSMS rotary system. Experimental results demonstrate that in addition to the type and order of the mapping function, the number and spatial arrangement of sensors are crucial in achieving nanodegree angular positional accuracy. While the focus articulated here is magnetic field-based sensing, this approach can potentially be extended to develop other sensing systems that capitalize on scalar (temperature), vector (electrostatic, gravitational), and even tensor (stress) fields.

REFERENCES

[1] F. H. Raab, E. B. Blood, T. O. Steiner, and H. R. Jones, "Magnetic position and orientation tracking system," *IEEE Trans. Aerospace Electron. Syst.*, vol. AES-15, no. 5, pp. 709–718, Sep. 1979.

[2] K.-M. Lee and D. Zhou, "A real-time optical sensor for simultaneous measurement of three-DOF motions," *IEEE/ASME Trans. Mechatronics*, vol. 9, no. 3, pp. 499–507, Sep. 2004.

[3] H. Garner, M. Klement, and K.-M. Lee, "Design and analysis of an absolute non-contact orientation sensor for wrist motion control," in *Proc. IEEE/ASME Int. Conf. Adv. Intell. Mechatronics*, Como, Italy, Jul. 2001, pp. 69–74.

[4] K.-M. Lee, K. Bai, and J. Lim, "Dipole models for forward/inverse torque computation of spherical motor," *IEEE/ASME Trans. Mechatronics*, vol. 14, no. 1, pp. 46–54, Feb. 2009.

[5] G. Krebs, A. Tounzi, B. Pauwels, D. Willemot, and F. Piriou, "Modeling of a linear and rotary permanent magnet actuator," *IEEE Trans. Magnetics*, vol. 44, no. 11, pp. 4357–4360, Nov. 2008.

[6] W. Wang, J. Wang, G. W. Jewell, and D. Howe, "Design and control of a novel spherical permanent magnet actuator with three degrees of freedom," *IEEE/ASME Trans. Mechatronics*, vol. 8, no. 4, pp. 457–468, Dec. 2003.

[7] K.-M. Lee, R. A. Sosseh, and Z. Wei, "Effects of torque model on the control of a VR spherical motor," *Control Eng. Practice*, vol. 12, pp. 1437–1449, 2004.

[8] L. Yan, I.-M. Chen, C. K. Lim, G. Yang, W. Lin, and K.-M. Lee, "Design and analysis of a permanent magnet spherical actuator," *IEEE/ASME Trans. Mechatronics*, vol. 13, no. 2, pp. 239–248, Apr. 2008.

[9] C. K. Lim and I. M. Chen, "A novel 3-DOF sensing methodology for spherical actuator," in *Proc. IEEE/ASME Adv. Intell. Mechatronics*, Zurich, Switzerland, Sep. 2007, pp. 1–6.

[10] J. Lenz and A. S. Edelstein, "Magnetic sensors and their applications," *IEEE Sensors J.*, vol. 6, no. 3, pp. 631–649, Jun. 2006.

[11] M. Caruso, T. Bratland, C. Smith, and R. Schneider, "A new perspective on magnetic field sensing," *Sensors Mag.*, vol. 15, pp. 34–45, Dec. 1998.

[12] Y. M. Choi and D.-G. Gweon, "A high precision dual-servo stage using Halbach linear active magnetic bearings," *IEEE/ASME Trans. Mechatronics*, in press.

[13] M.-C. Tsai and C.-C. Huang, "Development of a variable-inertia device with a magnetic planetary gearbox," *IEEE/ASME Trans. Mechatronics*. DOI: 10.1109/TMECH.2010.2077679, Nov. 11, 2010.

[14] M. Xu and N. Ida, "Solution of magnetic inverse problems using artificial neural networks," in *Proc. 6th Int. Conf. Optimization Electr. Electron. Equipments*, May 1998, vol. 1, pp. 67–70.

[15] J. T. Nenonen, "Solving the inverse problem in magnetocardiography," *IEEE Eng. Med. Biol. Mag.*, vol. 13, no. 4, pp. 487–496, Aug./Sep. 1994.

[16] V. Schlageter, P. Drljaca, R. S. Popovic, and P. Kucera, "A magnetic tracking system based on highly sensitive integrated hall sensors," *JSME Int. J., Series C: Mech. Syst., Machine Elements Manuf.*, vol. 45, no. 4, pp. 967–973, Dec 2002.

[17] C. Hu, M. Q.-H. Meng, M. Mandal, and X. Wang, "3-axis magnetic sensor array system for tracking magnet's position and orientation," in *Proc. 6th World Congr. Intell. Control Autom.*, Jun. 2006, pp. 5304–5308.

[18] J. T. Sherman, J. K. Lubkert, R. S. Popovic, and M. R. DiSilvestro, "Characterization of a novel magnetic tracking system," *IEEE Trans. Mag.*, vol. 43, no. 6, pp. 2725–2727, Jun. 2007.

[19] M.-C. Tsai and C.-H. Yang, "A flux-density-based electromagnetic servo system for real-time magnetic servoing/tracking," *IEEE/ASME Trans. Mechatronics*, vol. 13, no. 2, pp. 249–256, Apr. 2008.

[20] D. K. Cheng, *Field and Wave Electromagnetics*, MA: Addison-Wesley, 1989.

[21] W. S. Bennett, "Basic sources of electric and magnetic fields newly examined," *IEEE Antennas Propag. Mag.*, vol. 43, no. 1, pp. 31–35, Feb. 2001.

[22] K.-M. Lee and H. Son, "Distributed multipole model for design of permanent-magnet-based actuators," *IEEE Trans. Magn.*, vol. 43, no. 10, pp. 3904–3913, Oct. 2007.

This article has been accepted for inclusion in a future issue of this journal. Content is final as presented, with the exception of pagination.

10   IEEE/ASME TRANSACTIONS ON MECHATRONICS

[23] H. Son and K.-M. Lee, "Distributed multipole models for design and control of PM actuators and sensors," *IEEE/ASME Trans. Mechatronics*, vol. 13, no. 2, pp. 228–238, Apr. 2008.

[24] S. Foong, "Development of magnetic field-based multisensor system for multi-DOF actuators," Ph.D. dissertation, Georgia Tech, Atlanta, GA, USA, 2010.

Kun Bai (S'11) received the B.S. degree from Zhejiang University, Hangzhou, China, in 2006. He is currently working toward the Ph.D. degree in the George W. Woodruff School of Mechanical Engineering, Georgia Institute of Technology, Atlanta.

His research interests include automation, control systems, and mechatronics.

Shaohui Foong (M'06) received the B.S. and M.S. degrees in mechanical engineering in 2005 and 2008, respectively, from the George W. Woodruff School of Mechanical Engineering, Georgia Institute of Technology, Atlanta, and the Ph.D. degree from the Georgia Institute of Technology in 2010.

He is currently an Assistant Professor at the Singapore University of Technology of Design, Singapore, and a Visiting Scholar at the Massachusetts Institute of Technology, Cambridge. His research interests include system dynamics/control, distributed sensing, sensor fusion and automation.
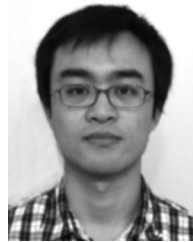
Kok-Meng Lee (M'89–SM'02–F'05) received the B.S. degree from the State University of New York, Buffalo, in 1980, and the S.M. and Ph.D. degrees from the Massachusetts Institute of Technology, Cambridge, in 1982 and 1985, respectively.

He is currently a Professor in the George W. Woodruff School of Mechanical Engineering, Georgia Institute of Technology, Atlanta. His research interests include system dynamics/control, robotics, automation, and mechatronics. He holds eight patents in machine vision, a 3-DOF spherical motor/encoder, and a live-bird handling system.

Dr. Lee is a Fellow of the ASME. He received the National Science Foundation (NSF) Presidential Young Investigator, Sigma Xi Junior Faculty Research, International Hall of Fame New Technology, and Kayamori Best Paper Awards.